THE JOURNAL OF PHYSICAL CHEMISTRY C

pubs.acs.org/JPCC Article

Effect of Second-Sphere Interactions on the Magnetic Anisotropy of Lanthanide Single-Molecule Magnets: Electrostatic Interactions and Supramolecular Contacts

Yolimar Gil, Leonel Llanos, Patricio Cancino, Pablo Fuentealba, Andrés Vega, Evgenia Spodine,* and Daniel Aravena*

Cite This: J. Phys. Chem. C 2020, 124, 5308−5320 Read Online

ACCESS | Metrics & More | Article Recommendations | Supporting Information

ABSTRACT: To study how second-sphere interactions affect single-molecule magnet (SMM) properties of mononuclear lanthanide systems, two dysprosium(III) complexes [Dy(*N*-NCS)$_3$(H$_2$O)$_5$]·0.45(KSCN)(18-crown-6) (**1**) and [Dy(NO$_3$)$_2$(*N*-NCS)$_3$(H$_2$O)]·(H$_2$O)-(NH$_4$)$_2$2(18-crown-6) (**2**) were synthesized and characterized by single-crystal X-ray diffraction, ac, dc magnetometry, and multireference ab initio calculations. For **1**, Dy^{III} complexes are encapsulated between two crown ether molecules, while crown ether molecules and Dy^{III} complexes crystallize in separate rows for **2**. Ab initio calculations indicate that encapsulation is detrimental for magnetic anisotropy in the case of **1**. This effect is related to a mismatch of the anisotropy axis of the Dy^{III} complex and the symmetry axis of the encapsulating crown ether molecules. Ab initio calculations show that the reorientation of the electrostatic potential exerted by the crown ethers to a more symmetric position produces an enhancement of magnetic anisotropy. We tested the general character of this effect by analyzing a reported Dy^{III} complex encapsulated by crown ether molecules. We also investigated how specific hydrogen-bond interactions affect magnetic anisotropy and show that H-bonds can be beneficial or prejudicial for magnetic anisotropy, depending on their position with respect to the magnetic axis. Our conclusions give general orientations about tuning intermolecular interactions to promote single-molecule magnet properties by controlling electrostatic and supramolecular interactions.

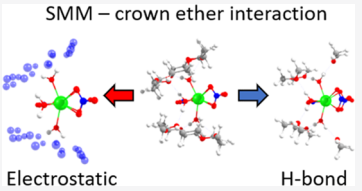

INTRODUCTION

The development of single-molecule magnets (SMMs) is one of the most rapidly growing areas within the field of molecular magnetism.[1−6] These molecular complexes exhibit slow relaxation of the magnetization in the absence of an applied field, due to the presence of an energy barrier to the reversal of magnetization.[7] In 2011, Rinehart and Long[8] proposed a simple electrostatic model for predicting the ligand architectures that will generate strong magnetic anisotropy for a variety of trivalent lanthanide ions based on their basic overall shape of free-ion electron density. Oblate electronic density (flattened spheroid observed for Nd^{III}, Tb^{III}, or Dy^{III}) is efficiently stabilized with an axial crystal field, while prolate density (elongated spheroid found for ions such as Er^{III}) requires stabilization in the equatorial plane.

Magnetization relaxation is governed by various mechanisms such as Orbach, Raman, direct relaxation, and quantum tunneling of the magnetization (QTM). The latter may reduce the efficiency of the SMM by involving direct transitions between the ground doublet $\pm m_J$ states. In Ln^{III}-based SMMs, tunneling relaxation is highly dependent on various parameters such as the dipolar interactions, hyperfine coupling,[9] magnetic exchange interactions,[10] and deviation from high symmetry.[11] In the latter case, the accurate control of the coordination environment of the lanthanide site, guided by the crystal field theory, could be used to minimize the QTM.[11]

Dy^{III} is the most commonly employed lanthanide cation due to the large magnetic moment for its Kramers' doublet ground state. To give a highly anisotropic ground state with a large $\pm m_J$, the Dy^{III} ion should be ideally surrounded by a linear or sandwich-type ligand geometry, maximizing the anisotropy of an oblate ion. However, such coordination geometries are difficult to synthesize since lanthanide ions tend to form complexes with high coordination numbers.[12] For this reason, macrocyclic ligands such as phthalocyanine (Pc) and its derivatives,[13−17] cyclooctatetraene (COT),[18−22] 1,4,7,10-tetraazacyclo-dodecane-1,4,7,10-tetraaceticacid (DOTA),[23] as well as polyoxometalates (POMs),[24,25] have been employed for the formation of sandwich-type Ln^{III} structures.

Crown ethers with small cavities such as 15-crown-5 and 12-crown-4 have been employed to obtain sandwich-type Ln^{III} structures. Specifically, a half-sandwich complex of 12-crown-4 with Dy^{III},[26] a pseudo-sandwich complex of 15-crown-5 with Dy^{III},[26] and a full-sandwich complex of 15-crown-5 with Sm^{III},[27] where in all cases the metal remains out of the central cavity of the crown ethers, have been reported. Among these systems,

Received: September 30, 2019
Revised: January 13, 2020
Published: February 13, 2020

https://dx.doi.org/10.1021/acs.jpcc.9b09234
J. Phys. Chem. C 2020, 124, 5308−5320

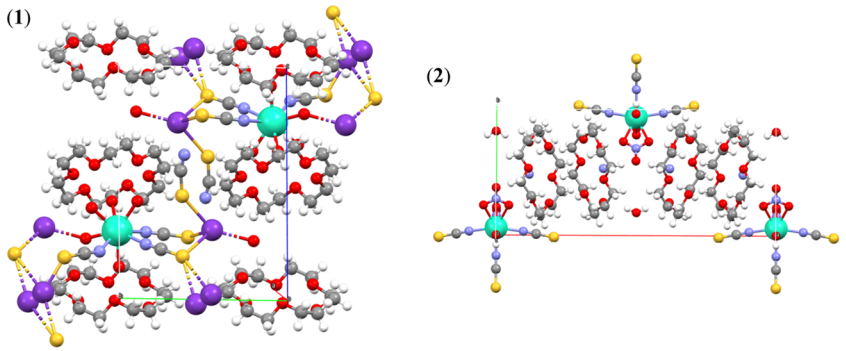

Figure 1. Packing view along [100] and [010] for the structure of $[Dy(N\text{-}NCS)_3(H_2O)_5]\cdot 0.45(KNCS)\cdot$(18-crown-6) (**1**) and $[Dy(NO_3)_2(N\text{-}NCS)_3(H_2O)]^{2-}$ (**2**), respectively. Color code: Dy (green), S (yellow), O (red), N (light blue), K (purple), C (gray), and H (white).

Dy^{III} complexes were shown to have mononuclear SMM behavior. On the other hand, crown ethers are also used for the preparation of outer-sphere adducts that are formed via noncovalent, hydrogen-bonding, and $\pi-\pi$ stacking interactions.[28] In this way, 15-crown-5 has been used to afford supramolecular 15-crown-5 Ln^{III} chains (Ln^{III} = Tb and Dy), where the metal complex molecules are not covalently but hydrogen-bonded to the crown ether ones. Magnetic studies show field-induced SMM behavior for the Dy^{III} complex but rapid relaxation of the magnetization for the Tb^{III} one.[29] Besides, benzo-15-crown-5 has been used to synthesize a Ln^{III}-based SMM, by encapsulation of the $[Dy(OH_2)_8]^{3+}$ cation between three macrocyclic units, which are hydrogen-bonded to the metal. Encapsulation results in long intermolecular Dy···Dy distances of >12 Å, analogous to magnetic dilution and is therefore a useful strategy for reducing dipolar interactions in the crystal lattice, which in turn may also suppress QTM.[30]

On the other hand, crown ethers with large cavities, such as 18-crown-6, have been used to obtain lanthanide complexes, where Ln^{III} remains inside the cavity.[31−34] The literature reports that 18-crown-6 also afforded supramolecular chains of metal complexes based on nonmagnetic Y^{III}, Sc^{III}, Ga^{III}, and In^{III}, which are hydrogen-bonded to 18-crown-6.[28,35,36] It has been demonstrated that modifications to the cavity of the crown ether ligand on sandwich-type Dy^{III} structures subtly affect the local symmetry of the Dy^{III} ions that in turn significantly affects the energy levels of Kramers' doublets, altering the relaxation pathways.[26]

Herein, we have considered the study of the influence of 18-crown-6 on the magnetic properties for different encapsulated dysprosium complexes. We prepared two different Dy^{III} complexes (**1** and **2**, respectively) obtained by the reaction between 18-crown-6 with $Dy(NO_3)_3\cdot 5H_2O$ and two different thiocyanate salts (KSCN, NH_4SCN).

Complex **1** shows encapsulation between crown ether ligands, while complex **2** is not encapsulated since crown ether molecules and Dy^{III} complexes crystallize in separate rows, as shown in Figure 1. Ab initio calculations show that encapsulation exerted a detrimental effect on magnetic anisotropy in the case of **1**. A similar behavior has been observed recently and was related to modifications of the electrostatic potential due to encapsulation.[37] Considering these findings, we investigated if the negative influence of the encapsulating crown ether ligands is a general result or can be reversed to enhance magnetic anisotropy instead of diminishing it. Complete active space self-consistent field (CASSCF) and density functional theory (DFT) calculations on X-ray and model structures were carried out to identify the origin of this second-sphere effect and identify the most favorable conditions for the SMM performance. We analyzed the electrostatic effect and specific supramolecular interactions (H-bonding) and identified structural conditions that promote magnetic anisotropy.

EXPERIMENTAL SECTION

Physical Measurements. The Fourier transform infrared (FT-IR) spectra were recorded using KBr pellets, in the range 400−4000 cm^{-1} on a Spectrum BX II FT-IR spectrometer (PerkinElmer). Elemental analyses were done on a Thermo Flash Analyzer, 2000 Series, with TCD detector.

Alternate (ac) and direct current (dc) magnetic susceptibility measurements were performed using a Quantum Design SQUID MPMS magnetometer. For ac measurements, an oscillating field of 4 Oe was selected, in the frequency range of 1−1500 Hz. Temperature-dependent (2−300 K) susceptibility was determined under a static field of 3000 Oe; the dc field for dynamic measurements was 1000 Oe for **1** and **2**.

Materials and Methods. All reagents and solvents were commercially available and used without further purification.

*Synthesis of $[Dy(N\text{-}NCS)_3(H_2O)_5]$ 0.45(KNCS)·(18-crown-6) (**1**).* KSCN (145.8 mg, 1.5 mmol) in 10 mL of anhydrous ethanol was added to a solution of $Dy(NO_3)_3\cdot 5H_2O$ (219.3 mg, 0.5 mmol) in 5 mL of the same solvent. The mixture was sonicated for 15 min, and a white precipitate corresponding to KNO_3 was formed immediately. The mixture was filtered, and the solution was added to a solution of 18-crown-6 (132.1 mg, 0.5 mmol) in 5 mL of anhydrous ethanol. The mixture formed a precipitate, which was filtered, and then the solid product was dissolved in 5 mL of acetonitrile. After slow evaporation of the solution at room temperature over about 1 week, pink crystals suitable for X-ray diffraction were obtained. Yield 0.26 g (35.88%). IR (KBr, cm^{-1}): 3362 (br, O−H); 2906 (m, C−H); 2052 (s, C ═ N); 1621 (w, H−O−H); 1471, 1351, 1288, 1249 (m, CH_2); 1108 (s, C−O−C); 961 (m, C−C); 835 (m, C═S). Anal. calcd for $C_{15.45}H_{34}DyN_{3.45}O_{11}S_{3.45}K_{0.45}$: C, 25.2; H, 4.6; N, 6.6; S, 15.0%. Found C, 26.6; H, 4.3; N, 6.6; S, 14.6%.

*Synthesis of $[Dy(NO_3)_2(N\text{-}NCS)_3(H_2O)]\cdot(H_2O)(NH_4)_2\cdot 2$(18-crown-6) (**2**).* NH_4SCN (114 mg, 1.5 mmol) in 10 mL of anhydrous ethanol was added to a solution of $Dy(NO_3)_3\cdot 5H_2O$ (219.3 mg, 0.5 mmol) in 5 mL of the same solvent. The mixture was sonicated for 15 min, then a solution of 18-crown-6 (132 mg, 0.5 mmol) in 5 mL of anhydrous ethanol was added, and the mixture was sonicated for 10 min, obtaining a light pink solution. Pink single crystals appeared from the solution after 1 week. Yield 0.24 g (45.30%). IR (KBr, cm^{-1}): 3424 (br, O−H); 3265,

https://dx.doi.org/10.1021/acs.jpcc.9b09234
J. Phys. Chem. C 2020, 124, 5308−5320

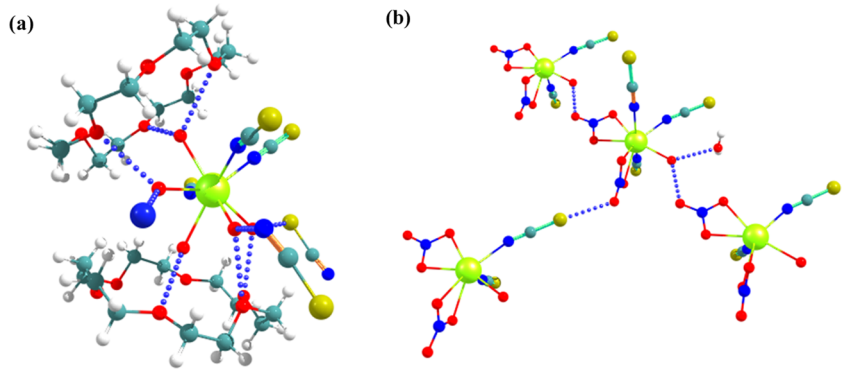

Figure 2. (a) Short contacts (blue dotted lines) from coordinated water molecules in $[Dy(N\text{-}NCS)_3(H_2O)_5]$ (**1**). (b) Hydrogen bonds from coordinated water and NO_3^- ligands in $[Dy(NO_3)_2(\text{-}N\text{-}NCS)_3(H_2O)]^{2-}$ (**2**). Color code: Dy (green), S (yellow), O (red), N (blue), C (gray), and H (white).

3176, 3053 (m, N−H); 2912 (m, C−H); 2082, 2038 (s, C═N); 1618 (w, H−O−H); 1441 (s, N═O); 1303 (s, NO_2); 1091 (s, C−O−C); 956 (m, C−C); 832 (m, C═S). Anal. calcd for $C_{27}H_{58}DyN_7O_{20}S_3$: C, 30.6; H, 5.6; N, 9.2%. Found C, 30.7; H, 5.6; N, 9.3%.

X-ray Crystallography. *Structural Determination.* The crystal structures for **1** and **2** were determined by X-ray diffraction at 293 K. Data collection was done on a SMART-APEX II CCD diffractometer system. Data were reduced using SAINT,[38] while the structures were solved by direct methods and subsequently completed by difference Fourier synthesis and refined by least squares using SHELXL.[39,40] Multiscan absorption corrections were applied using SADABS.[38] The hydrogen-atom positions were calculated after each cycle of refinement with SHELXL using a riding model for each structure, with a C−H distance of 0.93 Å. The $U_{iso}(H)$ values were set equal to $1.2U_{eq}$ of the parent carbon atom. Despite efforts, not all hydrogen atoms on the coordinated water molecules were located in the difference Fourier map. Those which were found were refined, subjected to the restriction of the distance to the water oxygen atom of 0.85 Å. For **1**, after the location of the complex $[Dy(N\text{-}NCS)_3(H_2O)_5]$ and a molecule of crown ether (rigorously two halves within the asymmetric unit), it was clear that some non-negligible electron densities remained within the space left by those. It was finally modeled as interstitial KSCN, whose occupancy was first refined and then held equal to 0.45. Within the asymmetric unit, there are two potassium-ion sites whose respective occupancies are 0.15 and 0.45. Table S1 shows the main data collection and refinement details for **1** and **2** and was prepared with publicif.[41]

Computational Details. Electronic structure calculations were performed using the ORCA 4.0.1.2 package.[42] The starting point for the construction of molecular models was the X-ray crystallographic structure. Two kinds of models were generated: (i) a "full" structure, considering one Dy^{III} complex and the two 18-crown-6 molecules surrounding it and (ii) a "small" model, just containing the complex. The full model was not constructed for **2** since this system is not encapsulated. In the case of **1**, sulfur and some carbon atoms from the crown ether were optimized by constrained structural relaxations based on the BP86 density functional[43,44] in conjunction with the all-electron Def2-TZVP basis set.[45] Dysprosium was described by the SARC2-QZVP basis set.[46] For all cases, hydrogen positions were relaxed under the same settings. Scalar relativistic effects were included by means of the DKH2 Hamiltonian.[47−49] It is important to note that small and full models are identical with respect to the common Dy^{III} complex. Thus, differences in electronic structure cannot be related to structural changes but to modifications in the wave function. State-averaged CASSCF(9,7)[50] calculations included the seven 4f orbitals of the Dy^{III} ion with 21, 224, and 490 sextet, quartet, and doublet roots, respectively. After convergence of CASSCF energies, spin−orbit coupling (SOC) effects were included in a subsequent quasi-degenerate perturbation theory (QDPT) step. β electron densities were calculated based on nonrelativistic (CASSCF) ground-state wave functions. Tunneling relaxation times were calculated according to a recently proposed model,[51] and input data for this methodology are the crystallographic information file, obtained from the Cambridge Crystallographic Database[52] and the CASSCF(9,7)/QDPT calculated g-tensor of the ground Kramers' doublet. Atomic charges representing the electrostatic potential were calculated by the CHELPG method[53] from the electron distribution obtained from a Hartree−Fock[54,55] calculation considering only the crown ether fragments. Atomic charges corresponding to hydrogen atoms were condensed to their bonded carbons. We employed this method instead of DFT since we are comparing with CASSCF calculations, where the orbitals associated with crown ether fragments are outside the active space. To avoid the presence of metal-centered low-lying excited orbitals, MP2 calculations were performed by replacing Dy^{III} with Y^{III}, where the basis set for this element was x2c-TZVPall.[56] Natural atomic charges were calculated using NBO 7.0.[57]

RESULTS AND DISCUSSION

Structural Description. Two Dy^{III} complexes coordinating small ligands such as thiocyanate, $[Dy(N\text{-}NCS)_3(H_2O)_5]$ (**1**), and a mixture of thiocyanate and nitrate, $[Dy(NO_3)_2(N\text{-}NCS)_3(H_2O)]^{2-}$ (**2**), were obtained by standard experimental procedures, just changing the cation of the thiocyanate salt (KSCN, NH_4SCN). All complexes present water ligands completing their coordination sphere. The crystalline lattice of **1** and **2** contains KSCN and NH_4^+, respectively. The proportion and relative orientation of the complexes and crown ether molecules are also different: **1** presents a 1:1 ratio between 18-crown-6 and the corresponding Dy^{III} complexes, where both fragments alternate in a sandwich arrangement. In the case of **2**, the Dy^{III}/18-crown-6 ratio is 1:2, without an alternating ordering (Figure 1).

The neutral or anionic complex moieties are $[Dy(N\text{-}NCS)_3(H_2O)_5]$ for **1** and $[Dy(NO_3)_2(N\text{-}NCS)_3(H_2O)]^{2-}$ for **2**. Table S2 shows the main distances and angles for each

https://dx.doi.org/10.1021/acs.jpcc.9b09234
J. Phys. Chem. C 2020, 124, 5308−5320

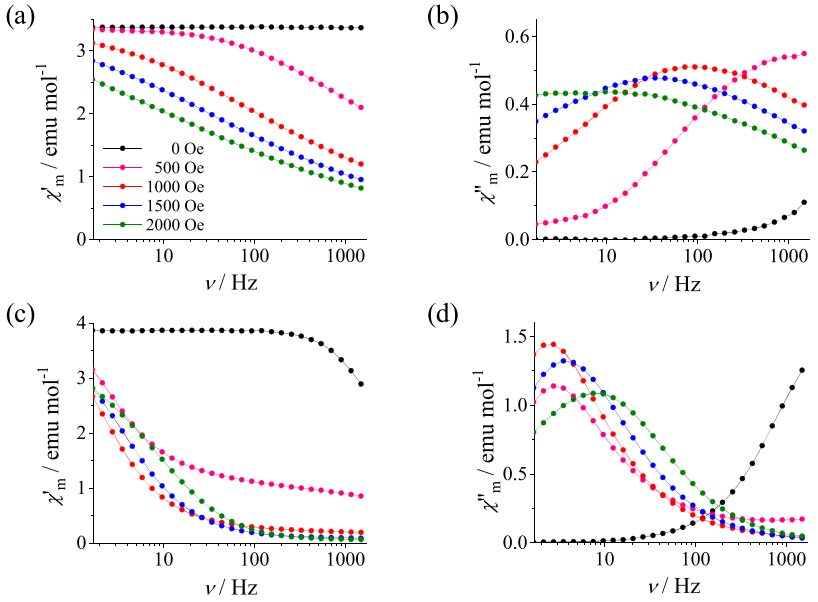

Figure 3. Frequency-dependent ac magnetic susceptibility for **1** (a, b) and **2** (c, d). χ' (left) and χ'' (right). Color code for dc fields: 0 Oe (black), 500 Oe (pink), 1000 Oe (red), 1500 Oe (blue), 2000 Oe (green). Measurements were performed at T = 3.5 K for **1** and 3 K for **2**.

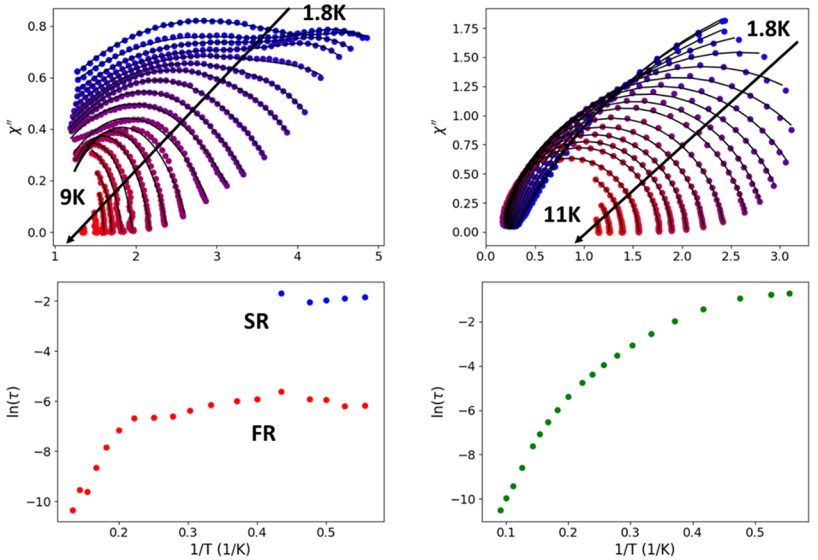

Figure 4. Top: Cole−Cole plots for **1** (left) and **2** (right). Temperature ranges are 1.8−9 K for **1** and 1.8−11 K for **2**. Lower temperatures are represented in blue, and higher temperatures in red. Fitted curves are presented as black lines. Bottom: ln(τ) vs 1/T relations for **1** (left) and **2** (right).

complex. Complexes $[Dy(N\text{-}NCS)_3(H_2O)_5]$ (**1**) and $[Dy(NO_3)_2(N\text{-}NCS)_3(H_2O)]^{2-}$ (**2**) have an octacoordinated Dy^{III} center, where three of the coordinated positions correspond to monodentate *N*-thiocyanate anions, while the remaining five positions are occupied by water molecules in **1** or two *O*,*O*′-nitrate groups and a water molecule in **2**. The use of the SHAPE code[58] allowed the calculation of the coordination modes of these complexes. Although highly distorted, the coordination geometry for **1** can be described as a square antiprism (S = 0.394), while that of **2** as a triangular dodecahedron (S = 1.938). The uncoordinated sulfur atoms of the thiocyanate anions are implied in intermolecular interactions. Within the crystal structure of **1**, the lanthanide-containing complexes of $[Dy(N\text{-}NCS)_3(H_2O)_5]$ alternate with potassium cations (Figure S1a) along the [010] direction (Figure S1b), defining a sort of chainlike arrangement, while the 18-crown-6 organic molecules lie in the space between those (Figure S1c). In contrast, Shiping et al.[59] and Bakker et al.[60] have previously described the Dy^{III} center coordinated by the crown ether in $[Dy(NCS)_3(\text{dibenzo-30-crown-10})(H_2O)_2]$ and $[Dy(NCS)_3(\text{18-crown-6})]$, respectively. For the case of **2**, hydrogen bonds exist between the water molecules coordinated to dysprosium and the solvating one, as shown in Figure 2b and stated in Table S3. In the case of complex **1**, it is important to emphasize that there are some short contacts between coordinated water and ether oxygen atoms (i.e., O1w O13 2.785 Å and O1w O15vi 2.942 Å, where vi = 1 - x, $-y$, 2 − z), that suggest the existence of hydrogen bonds (Figure 2a). Despite several efforts, the implied water hydrogen atoms were not confidently located into the difference Fourier map. The existence of Werner-type complex molecules of Dy^{III} co-crystallized with organic molecules of 18-crown-6 and anions or cations within the crystal packing of each one of the compounds

https://dx.doi.org/10.1021/acs.jpcc.9b09234
J. Phys. Chem. C 2020, 124, 5308−5320

makes the intermetallic distances very long. The shortest values are 8.273(1) Å (Dy1···Dy1 $1 - x, -y, 2 - z$) and 8.490(4) Å (Dy1···Dy1 $x, y, 2 + z$) for **1** and **2**, respectively.

Magnetic Properties. Magnetic susceptibilities for **1** and **2** at a constant field of 3000 Oe in the temperature range of 2−300 K are presented in Figure S3. As expected, the χT value at high temperature for both complexes is close to the free-ion value for a Dy^{III} center (14.17 cm^3 K mol^{-1}). Below 100 K, χT smoothly decreases to values around 10 cm^3 K mol^{-1} at 2 K, due to the depopulation of the excited states belonging to the ground $^6H_{15/2}$ multiplet. The field dependence of the magnetization measured at 2 K (Figure S4) for complexes **1** and **2** show a rapid increase of magnetization below 1 T and then a very slow linear increase to reach values of 5.4 NμB (**1**) and 5.3 NμB (**2**) at 5 T.

Field-dependent (ac) magnetic susceptibility curves are presented in Figure 3. At zero field, χ'' was always close to zero and presents only a weak frequency dependence in the 1−1500 Hz range. The inclusion of a static magnetic field in the range of 500−2000 Oe allows the observation of a peak. We chose 1000 Oe as a convenient field to measure frequency- and temperature-dependent susceptibility since this field allows for the observation of intense χ'' curves for both complexes, with a maximum inside the ac frequency range.

Cole−Cole plots for **1** and **2** are presented in Figure 4. In the case of **1** (Figure 4, left), a single relaxation process is observed at higher temperatures (9−3 K), while lower-temperature curves (2.7−1.8 K) show the presence of a second maximum that appears as a broad semicircle, heavily overlapping with the first signal. Relaxation times for slow and fast relaxation processes (labeled as SR and FR in Figure 4) were fitted to two modified Debye functions. The optimal parameters for all temperatures are presented in Table S5. The SR process is temperature-independent in the low-temperature range and then merges with the semicircle corresponding to the FR process, which dominates. The FR process presents a plateau a low temperature, then a linear dependence with respect to $1/T$. This suggests the presence of thermally activated relaxation, with a rough estimate of the barrier of 47 K (32 cm^{-1}). This value is small and consistent with ab initio calculations (vide infra).

Complex **2** presents a Cole−Cole plot (Figure 4, right) featuring one relaxation process. Temperature dependence of the relaxation time shows a non-Arrhenius behavior, which is commonly attributed to Raman relaxation.[61] A fit of the inverse relaxation time to a sum of tunneling ($1/\tau_{QT}$), Raman (CT^n), and Orbach ($\exp(-U_{eff}/T)/\tau_0$) terms affords the parameters $\tau_0 = 1.2 \times 10^{-7}$ s, $U_{eff} = 65.9$ K, $C = 0.022$ s^{-1} $K^{-5.67}$, $n = 5.67$, and $\tau_{QT} = 0.58s$. According to the classical model for two-phonon Raman relaxation,[62] n should be 7 for the first-order process in a Kramers ion. Deviations from this ideal behavior are usually attributed to thermalization dynamic processes.[34] The effective demagnetization barrier is still small but larger than **1**, again in agreement with theoretical results.

Electronic Structure Calculations. Complete active space self-consistent field (CASSCF) calculations were performed for **1** and **2**. We also calculated a recently reported Dy^{III} complex encapsulated by crown ether molecules,[37] $[Dy(NO_3)_3(H_2O)_3]$ (18-Crown-6), which is denoted **3**. We considered this additional system to check how general were the encapsulation effects observed for **1**. Calculated state energies and ground-state spin-Hamiltonian parameters are summarized in Table 1. In the case of **1** and **3**, three models were constructed: one with the isolated molecule (small), another considering two encapsulated crown ether molecules (full), and a model where atoms belonging to crown ether molecules are replaced by atomic charges ("ESP"). The small and full models are depicted in Figures 5−7. Further methodologic information is provided in the Computational Details section.

Table 1. Ab Initio First Excitation Energies (E_1) and Ground Doublet Spin-Hamiltonian Parameters for All Structural Models

			g-values		
		E_1	g_x	g_y	g_z
1	small	88.9	0.049	0.097	19.439
	full	46.4	0.200	0.342	18.870
	ESP	67.4	0.101	0.115	19.239
2	small	124.8	0.042	0.089	19.508
3	small	85.4	0.052	0.121	19.457
	full	43.2	0.135	2.521	16.193
	ESP	27.1	0.395	0.906	18.429

Results for the small model of **1** (Figure 5) indicate a moderate first excitation energy after the inclusion of spin−orbit coupling (SOC) effects (88.9 cm^{-1}), while the crystal field splits the $^6H_{15/2}$ ground multiplet by 525.6 cm^{-1}. This splitting is consistent with the weak ligand field associated with coordination complexes based on lanthanide(III) ions. The ground Kramers' doublet presents easy-axis magnetic anisotropy ($g_z = 19.439$) with small but non-negligible transverse components ($g_x = 0.049$ and $g_y = 0.097$). Comparing with other mononuclear dysprosium SMMs,[63] these values are consistent with field-induced slow relaxation of the magnetization. The second Kramers' doublet has large transverse components ($g_x = 1.108$ and $g_y = 2.132$) and a fast tunneling demagnetization time ($10^{-8.17}$ s). Demagnetization pathway calculations indicate that the second excited state dominates thermally assisted quantum tunneling relaxation (see Figure S6).

The calculated first excitation energy decreases to 46.4 cm^{-1} for the full model. Furthermore, the ground Kramers' doublet loses axiality ($g_x = 0.200$, $g_y = 0.342$, $g_z = 18.870$) and the total splitting of the $^6H_{15/2}$ ground multiplet diminishes to 468.3 cm^{-1}. Consequently, tunneling time for the ground state is faster than in the small model ($10^{-6.51}$ and $10^{-5.48}$ s, respectively). As lower excited states are more compressed in this case, second, third, and fourth excited states contribute to the thermally assisted tunneling (see Figure S6). In summary, calculations suggest that encapsulation is exerting a detrimental effect for the SMM properties of the system.

The direction of the ground-state magnetic moment lies close to that of the SCN ligands placed in a trans-position, with an SCN-Dy-NCS angle of 142.2° (Figure S7). This orientation of the magnetic moment suggests that the SCN ligands are associated with a stronger ligand field than that for water ligands. In this way, electron density from the 4f electrons will avoid the SCN axis, concentrating in the perpendicular plane and orienting the orbital angular momentum toward the more repulsive axis. The inclusion of encapsulating crown ether molecules does not change this general orientation, although some displacement of the vector is observed (25°). To check this analysis, the electron density of the two β electrons was plotted for each model (pink surfaces in Figures 5−7). In all cases, the density showed strong deviations from oblate shape, which is consistent with the significant transverse components of the observed g vectors.

In the case of **2**, (Figure 6) $[Dy(NO_3)_2(N\text{-}NCS)_3(H_2O)]^{2-}$ and crown ether molecules crystallize as separate rows, so there

https://dx.doi.org/10.1021/acs.jpcc.9b09234
J. Phys. Chem. C 2020, 124, 5308−5320

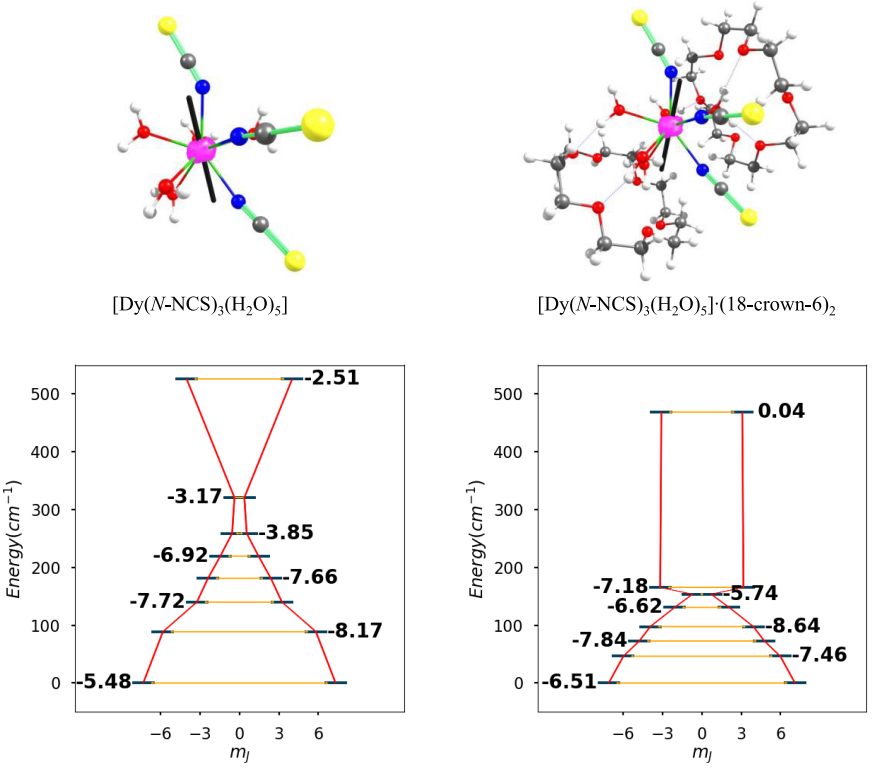

Figure 5. Top: Molecular structure of small (left) and full (right) models for **1**. Color code: S (yellow), O (red), N (blue), C (gray), and H (white). The g_z vector for the ground state is indicated as a black line, and the CASSCF ground-state β electron density is plotted as a pink surface. Bottom: ab initio state energies, m_j values, and tunneling relaxation times for the eight lowest Kramers' doublets of **1**. The blue bars indicate energies, the orange lines indicate tunneling pathways, while the numbers in black are the logarithm of the tunneling relaxation time (τ_{QTM}) for each Kramers' doublet.

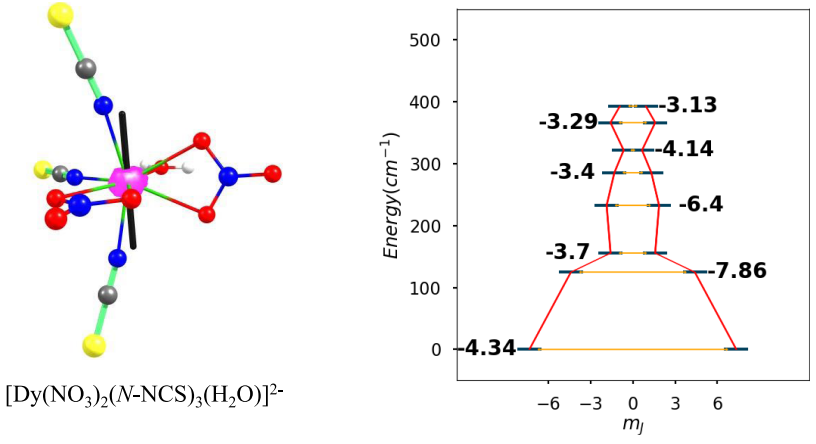

Figure 6. Left: Molecular structure of small model for **2**. Color code: S (yellow), O (red), N (blue), C (gray), and H (white). The g_z vector for the ground state is indicated as a black line, and the CASSCF ground-state β electron density is plotted as a pink surface. Right: ab initio state energies, m_j values, and tunneling relaxation times for the eight lowest Kramers' doublets of **1**. The blue bars indicate energies, the orange lines indicate tunneling pathways, while the numbers in black are the logarithm of the tunneling relaxation time (τ_{QTM}) for each Kramers' doublet.

is no encapsulation for this system. Thus, only the small model was calculated. Complex **2** is more axial than **1**, with a first excitation energy of 124.8 cm^{-1}, g_x = 0.042, g_y = 0.089, and g_z = 19.508. This is consistent with the observed field-induced SMM behavior. The ground $^6H_{15/2}$ multiplet is weakly split by 393.3 cm^{-1}; g_z aligns with the axis formed by the SCN ligands due to the higher ligand field originating from these ligands. The first excited state presents the fastest tunneling rate and dominates thermally assisted tunneling (see Figure S6).

Complex **3** is far from axiality, according to calculations. The encapsulated model presents relatively large transverse components of g, hampering the possibility to observe slow relaxation of the magnetization for this case (g_x = 0.135, g_y = 2.521, g_z = 16.193). Furthermore, the first excitation energy is markedly small (43.2 cm^{-1}). Again, the effect of crown ethers seems to be prejudicial for axial magnetic anisotropy. The small model shows significantly more axial g-vectors (g_x = 0.052, g_y = 0.121, g_z = 19.457), probably compatible with field-induced SMM properties. In addition, the first excitation energy is larger upon the removal of crown ethers (85.4 cm^{-1}). Interestingly, the direction of the magnetic moment is heavily distorted by encapsulation (Figure 7).

https://dx.doi.org/10.1021/acs.jpcc.9b09234
J. Phys. Chem. C 2020, 124, 5308−5320

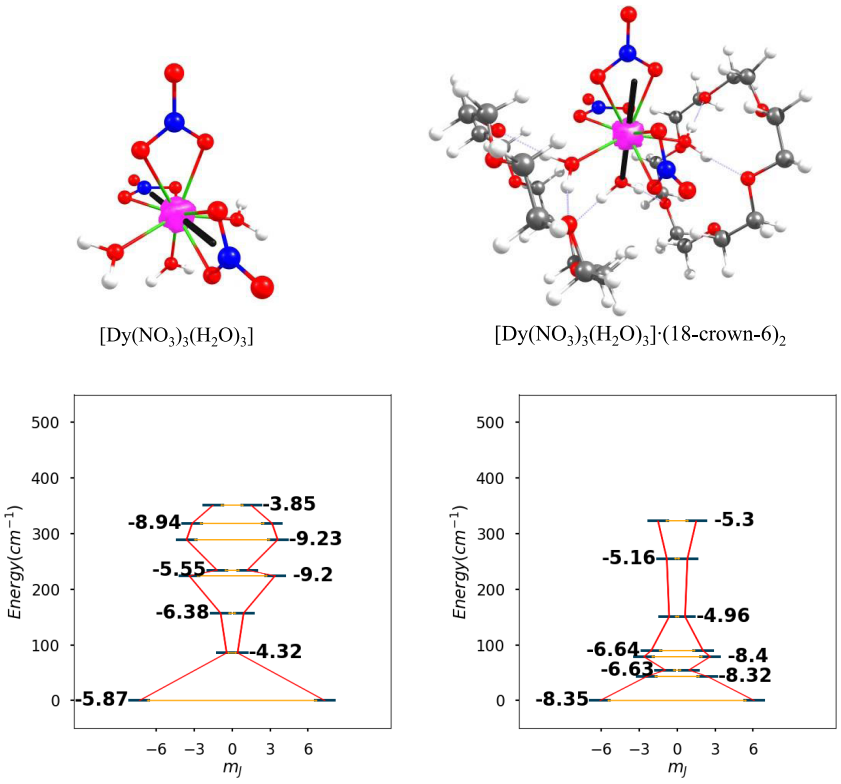

Figure 7. Top: Molecular structure of small (left) and full (right) models for **3**. Color code: S (yellow), O (red), N (blue), C (gray), and H (white). The g_z vector for the ground state is indicated as a black line, and the CASSCF ground-state β electron density is plotted as a pink surface. Bottom: ab initio state energies, m_j values, and tunneling relaxation times for the eight lowest Kramers' doublets of **1**. The blue bars indicate energies, the orange lines indicate tunneling pathways, while the numbers in black are the logarithm of the tunneling relaxation time (τ_{QTM}) for each Kramers' doublet.

Tunneling relaxation times were calculated according to a recently proposed model.[51] As the model is designed for relaxation times at zero field, and we are dealing with field-induced SMMs, calculated relaxation times should be associated with frequencies higher than the ac susceptibility window limit, preventing a direct comparison with experimental data. However, relative trends should be reasonably captured by the model. Considering the calculated tunneling times for the small models, complex **2** presents the slowest tunneling relaxation ($\tau = 4.5 \times 10^{-5}$ s), complex **1** is intermediate ($\tau = 3.3 \times 10^{-6}$ s), while **3** presents the fastest tunneling relaxation ($\tau = 1.3 \times 10^{-6}$ s). Comparing tunneling relaxation times from small and "large" models, we estimate that encapsulation significantly enhances tunneling relaxation for **1** and **3** by 1 and 2 orders or magnitude to $\tau = 3.1 \times 10^{-7}$ and 4.4×10^{-9} s, respectively.

For complex **3**, the angle between the magnetic moment vectors for the small and full models is 78.54°. For the small model, g_z points toward the two NO_3^- ligands placed in trans conformations. The hard plane is composed of three water molecules and the remaining NO_3^- ligand. The NO_3^- ligand exerts a larger ligand field splitting than water ligands. In this way, the oblate electron density prefers to orient toward water molecules, directing the magnetic moment in the perpendicular axis. Contrastingly, the full model has a magnetic moment pointing to one water and one NO_3^- ligand, while the hard plane is composed of two water and two NO_3^- ligands. Qualitatively, one may think that water ligands are becoming more repulsive and can now compete with the NO_3^- groups, reorienting the magnetic moment. As expected, the orientation of β electron density is heavily distorted upon the removal of the crown ether molecules, following the abrupt change in the orientation of g_z.

Comparing **1** and **3**, we observe that crown ether encapsulation worsened the SMM properties for both cases. The generality of this behavior will be examined in detail later. On the other hand, the strong magnetic moment reorientation observed in **3** was significantly smaller than that for **1** (79 and 25°, respectively). This difference can be explained by analyzing the symmetry of the coordination environment. In the case of **3**, NO_3^- and water ligands are organized like the vertices of an octahedron. Thus, three axes can be clearly defined: one with two NO_3^- ligands, expected to be the most repulsive, another with two water ligands (weakest), and one axis mixing water and NO_3^- ligands (intermediate). Hydrogen-bonding interactions will affect these axes differently, changing the balance between their ligand field effects and allowing for a strong magnetic moment reorientation. In contrast, there are no clearly repulsive axes **1**, as five water molecules and three thiocyanate ligands are coordinated in a geometry close to square antiprism. Angles between thiocyanate ligands are 76, 79, and 142° (Figure S7, top); the last value is far from describing opposing ligands. Even if these thiocyanates are considered to form a repulsive axis, the remaining SCN^- ligand does not have an opposing water ligand, where the largest SCN-Dy-OH_2 angles are 147, 137, and 118° (Figure S7, bottom), respectively. In summary, magnetic anisotropy of **1** will be affected by encapsulation since crucial H-bond interactions are present in this complex. However, these interactions lack the directionality needed for a strong reorientation of the magnetic moment.

As mentioned in the structural analysis, there are several hydrogen-bonding interactions between Dy^{III} complexes and crown ether molecules. These interactions are expected to influence magnetic anisotropy since they affect the electron

https://dx.doi.org/10.1021/acs.jpcc.9b09234
J. Phys. Chem. C 2020, 124, 5308−5320

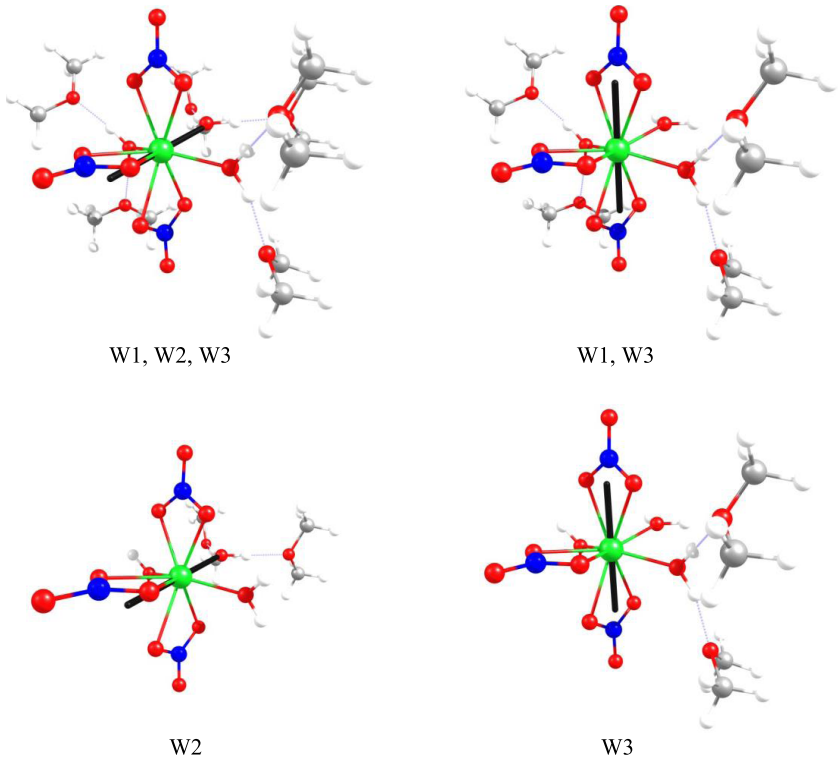

Figure 8. Magnetic moment orientation (black line) for selected simplified models of complex **3**.

density of water ligands bonded to the magnetic center. At the same time, the electrostatic field from crown ethers should also modulate magnetic anisotropy.[64] In practice, both effects will act simultaneously and are impossible to disentangle. We employ electronic structure calculations to analyze electrostatic and H-bonding interactions in model systems, trying to focus on them in a more separate way.

First, CASSCF calculations for the full models of **1** and **3** were modified by replacing the crown ether molecules by atomic charges, fitted to resemble the electrostatic potential (ESP models). Table 1 shows that magnetic anisotropy for ESP models is intermediate between small and full calculations. Despite this marked effect, the orientation of g_z was unaltered in comparison to the small model, not following the strong reorientation observed for the full model of **3**. In this way, the electrostatic potential is at least partly responsible for the lower axiality of the encapsulated models. Thus, magnetic moment reorientation must be related to effects beyond electrostatic interaction.

We then focused on weak interactions between Dy^{III} complexes and crown ethers. We performed MP2 calculations where Dy^{III} ions were replaced by Y^{III} to avoid the presence of low-lying metal virtual orbitals due to the combination of the weak ligand field, typical for lanthanide ions, and a single-reference wave function. These orbitals are irrelevant on the supramolecular interaction but will result in convergence difficulties and affect the perturbative MP2 treatment. Table S4 presents natural atomic charges for oxygen donor atoms from water ligands in the small and full models. For both **1** and **3**, there is a relatively small charge transfer from the crown ether to the molecule (0.11 and 0.14 e^-, respectively). This extra electron density is not evenly distributed in the complex and concentrates on the oxygen atoms from water ligands, which rise their electron count to 0.036, 0.050, and 0.036 electrons for complex **3**. Other molecular fragments as the Y^{III} ion or the NO_3^- ligands change their charges less than 0.01 e^- in all cases. The water ligand with the largest change in its molecular charge when comparing small and full models is the one interacting through hydrogen bonds with both crown ethers at the same time, denoted as W2 in Figure S5. This ligand is particularly important since it occupies the position where the magnetic moment is reoriented after crown ether encapsulation. For complex **1**, water ligands tend to concentrate the charge transfer, but the magnitude of the effect is more diluted than in **3**. This can be related to a better orientation of water ligands for H-bond formation in **3**. Summarizing results from electrostatic point charge models and the MP2 analysis of weak interactions, we see that both electrostatic and supramolecular interactions affect magnetic anisotropy in a simultaneous way. Magnetic moment reorientation in **3** is related to specific H-bond interactions rather than the bare electrostatic effect, which seems to be effective in reducing the overall magnetic anisotropy, but without inducing a significant magnetic moment reorientation.

To test the effect of hydrogen-bond interactions, we constructed a simplified model for **3** where the crown ethers were fragmented in dimethyl ether moieties (see Figure 8). Each crown ether molecule was fragmented in three sections, preserving all of the oxygen atoms involved in H-bonding (W1, W2, and W3 models in Figure 8). Then, different combinations of dimethyl ether fragments were removed to test how specific hydrogen bonds are affecting magnetic axiality. If all H-bond contacts are eliminated, the small model is obtained. *g*-values from these simplified models are intermediate between small and full models, suggesting that H-bond interactions explain part of anisotropy deterioration due to encapsulation, but electrostatic interaction also plays a role in this effect.

Table 2 presents *g*-values for models with different numbers of H-bond interactions. Interestingly, H-bonding to one of the

https://dx.doi.org/10.1021/acs.jpcc.9b09234
J. Phys. Chem. C 2020, 124, 5308−5320

Table 2. CASSCF Spin-Hamiltonian Parameters for Simplified Models of 3

H-bonding interactions	g_x	g_y	g_z	$\sqrt{g_x^2 + g_y^2}$
W1, W2, W3	0.097	0.463	18.089	0.473
W1, W2	0.014	0.369	18.440	0.370
W1, W3	0.046	0.112	19.172	0.121
W2, W3	0.012	0.364	18.442	0.364
W1	0.068	0.119	19.382	0.137
W2	0.035	0.266	18.534	0.269
W3	0.069	0.120	19.379	0.139
none	0.052	0.121	19.457	0.132

water ligands (W2) seems to account for most of the second-sphere effect. The magnitude of the transverse components of g ($\sqrt{g_x^2 + g_y^2}$) diminished from 0.473 to 0.121 when the hydrogen-bond interactions to W2 are removed. The change in g upon removal of H-bond interactions with other water ligands is minor (0.364 and 0.370 for W1 and W3, respectively). The same trend is observed if two water ligands are free from H-bond interactions. The model only retaining W2 has a large transverse component of g (0.269), while other models are lower (0.137 and 0.139). Consistent with MP2 calculations, W2 is the water ligand which receives the largest charge transfer from the crown ether fragments. The direction of the magnetic moment highlights the role of W2 controlling magnetic anisotropy as all models including H-bond interactions to this ligand show a magnetic moment aligned with the NO_3-Dy-OH_2 axis, while models lacking these interactions align their magnetic moment as the small model for **3** (see Figure 8).

To test this idea, we considered a model where the OC_2 plane of the dimethyl ether fragments corresponding to the sensitive water ligand (W2) was rotated every 10° to complete 90°, breaking the HO−H···OMe_2 contacts, without removing the fragment. In this way, the chemical interaction is broken but the electrostatic potential at the Dy^{III} position is not strongly affected since the rotation does not displace the second-sphere ether fragment in a drastic way (see Figure 9). Table 3 presents

Table 3. Variation in Ground-State g-Values upon Rotation of the Dimethyl Ether Fragments Associated with the Magnetically Relevant Water Ligand W2

rotation angle (deg)	g_x	g_y	g_z	$\sqrt{g_x^2 + g_y^2}$
0	0.035	0.266	18.534	0.269
10	0.106	0.641	17.720	0.649
20	0.266	1.766	15.768	1.786
30	0.321	1.770	16.417	1.799
40	0.213	0.793	18.342	0.821
50	0.143	0.428	18.979	0.451
60	0.108	0.290	19.199	0.310
70	0.092	0.233	19.287	0.250
80	0.084	0.210	19.321	0.226
90	0.081	0.204	19.330	0.219

the change in g-values upon rotation. At small angles (10−30°), axiality is markedly diminished, reaching a maximum $\sqrt{g_x^2 + g_y^2}$ of 1.8 at 30°. At higher angles, axiality is restored and even surpasses the initial value. The drastic variation of g-values is accompanied by a reorientation of the magnetic moment direction, as when crown ether molecules are removed from the full model.

Considering that H-bond interactions to aquo groups directly coordinated to the magnetic ion will result in an increase of the

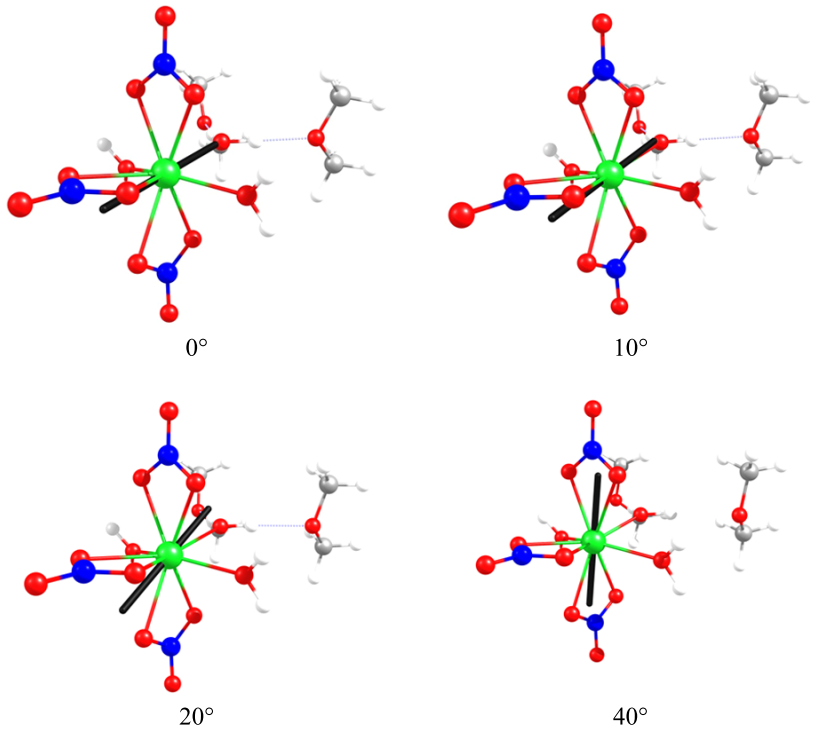

Figure 9. Variation in magnetic moment orientation values (black line) upon rotation of the dimethyl ether fragments associated with the magnetically relevant water ligand W2. After 40°, the direction of the magnetic moment remains pointing in the same direction.

https://dx.doi.org/10.1021/acs.jpcc.9b09234
J. Phys. Chem. C 2020, 124, 5308−5320

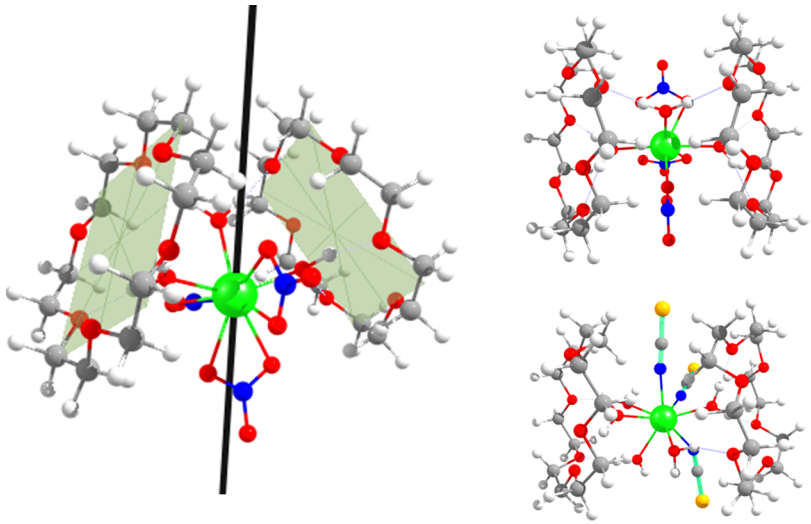

Figure 10. Left: Molecular structure of **3**. Crown ether planes are indicated as gray surfaces, and the C_2 axis is marked as a black line. Right: View along the C_2 axis or **3** (top) and **1** (bottom). In the case of **1**, the C_2 axis is approximate since both crown ether molecules are not symmetry-related.

negative charge on this ligand, the net effect of this contact will depend on the position of the water with respect to the magnetic moment axis. For an oblate ion, an increase of the repulsion of a ligand will be beneficial as long as it is oriented along the easy axis. The opposite will happen if the ligand is placed in the equatorial plane. In systems with high axiality, more repulsive ligands are oriented along the easy axis, while the weaker ones are in the plane. Water is a relatively weak ligand in comparison to other common groups in lanthanide SMMs. Thus, aquo ligands are expected to appear more on the equatorial plane than on the easy axis in favorable SMM environments. Consequently, H-bond interactions to water ligands will tend to be detrimental for SMM properties in most cases, as observed in the presented examples. An example of the key role of the secondary coordination sphere in controlling the magnetic moment and magnetization reversal barrier (U_{cal}) was reported by Murrie et al.[65] These authors calculated a number of different model systems created by the step-by-step elimination of each fragment of two Dy^{III} complexes. They demonstrated that the removal of anions/molecules in the secondary coordination sphere, which are hydrogen-bonding to equatorial coordinated water molecules, causes a lowering of the charges in the equatorial region around Dy^{III} ion and thus increases the axiality, enhancing the computed values of $U_{cal.}$

We now focus on tuning electrostatic interactions aiming to enhance magnetic axiality. From the analysis of crystallographic structures of **1** and **3**, we observe that the planes of both crown ethers are not parallel but form an angle of 37 and 50°, respectively. A parallel ("sandwich") disposition of two planar molecules (say, belonging to a D_{nh} point group) will generate nC_2 axis in the plane intermediate to both molecules. If both planes are not parallel (resembling more a "kebab"), only one of the C_2 axes will survive, determining the axial orientation of this fragment (see Figure 10). The dependence of the total symmetry in terms of the symmetry of its fragments and their relative orientation is named concurrent symmetry.[66] Observing through this approximate C_2 axis, we note that the disposition of **3** is more symmetric than **1**, since oxygen and carbon atoms are confronted in the first structure but are "twisted" in the second (see Figure 10). The higher symmetry of **3** allows for the comparison of the symmetry axis of the crown ether fragments and the magnetic axis of this complex. Interestingly, the C_2 axis of the crown ether is midway between the small and full anisotropy axes. From the ESP model of **3**, we reoriented the electrostatic potential by 59.3° to align the C_2 axis of the crown ethers with the NO_3-Dy-NO_3 axis. When the electrostatic potential is aligned with the NO_3^- ligand axis, magnetic anisotropy is more axial than that of the "small model" (g_x = 0.030, g_y = 0.064, and g_z = 19.422).

CONCLUSIONS

The use of thiocyanate salts with different cations allowed us to obtain dysprosium(III) complexes that have different first and second coordination spheres. Mononuclear complexes **1** and **2** were characterized as field-induced single-molecule magnets. Theoretical calculations agree with the observed magnetic behavior, describing a fast quantum tunneling, due to the presence of significant transverse anisotropy in the ground state. Calculations show that crown ether encapsulation is exerting a detrimental effect on the SMM properties since second-sphere interactions tend to lower the magnetic axiality in these cases. The origin of this effect is attributed to a combination of electrostatic effects and H-bond interactions, which augments the ligand field splitting associated with water ligands. In the case of complex **3**, a strong reorientation of ground-state magnetic moment is calculated, due to the presence of the encapsulating crown ether molecules. In most cases, H-bond interaction to aquo ligands will be detrimental for SMM properties, due to the charge transfer associated with H-bonding to a relatively weak ligand, which will be normally placed on the hard-magnetic plane for an oblate ion. Regarding electrostatic interactions, the alignment of the symmetry axis of the potential with the anisotropy axis of the system showed to be beneficial for enhancing magnetic anisotropy. A mismatch will have a negative effect, as observed experimentally.

ASSOCIATED CONTENT

Supporting Information

The Supporting Information is available free of charge at https://pubs.acs.org/doi/10.1021/acs.jpcc.9b09234.

https://dx.doi.org/10.1021/acs.jpcc.9b09234
J. Phys. Chem. C 2020, 124, 5308−5320

Crystallographic structures, magnetization and magnetic susceptibility data, ac susceptibility parameters, and detailed theoretical results (PDF)

AUTHOR INFORMATION

Corresponding Authors

Evgenia Spodine − *Facultad de Ciencias Químicas y Farmacéuticas, Universidad de Chile, CEDENNA, Santiago 8380494, Chile*; Email: espodine@ciq.uchile.cl

Daniel Aravena − *Departamento de Química de los Materiales, Facultad de Química y Biología, Universidad de Santiago de Chile, Santiago 9170022, Chile*; orcid.org/0000-0003-3140-4852; Email: daniel.aravena.p@usach.cl

Authors

Yolimar Gil − *Facultad de Ciencias Químicas y Farmacéuticas, Universidad de Chile, CEDENNA, Santiago 8380494, Chile*

Leonel Llanos − *Departamento de Química de los Materiales, Facultad de Química y Biología, Universidad de Santiago de Chile, Santiago 9170022, Chile*

Patricio Cancino − *Facultad de Ciencias Químicas y Farmacéuticas, Universidad de Chile, CEDENNA, Santiago 8380494, Chile*

Pablo Fuentealba − *Facultad de Ciencias Químicas y Farmacéuticas, Universidad de Chile, CEDENNA, Santiago 8380494, Chile*

Andrés Vega − *Departamento de Ciencias Químicas, Universidad Andrés Bello, CEDENNA, Santiago 8370011, Chile*; orcid.org/0000-0001-6501-4161

Complete contact information is available at: https://pubs.acs.org/10.1021/acs.jpcc.9b09234

Notes

The authors declare no competing financial interest.

ACKNOWLEDGMENTS

Y.G. and L.L. thank Conicyt for the National Doctoral Grant Nos. 21170520 and 21180269, respectively. P.F. thanks Fondecyt Postdoctoral Grant No. 3170186. The authors thank Projects FONDECYT 1170524 and Anillo ACT 1404 IPMAG, E.S. and A.V. Financiamiento Basal Proyecto FB0807 (CEDENNA), for financial support. Powered@NLHPC: This research was partially supported by the supercomputing infrastructure of the NLHPC (ECM-02). The authors thank Dr. Núria Clos from the University of Barcelona for the magnetic measurements and Dr. Poldie Oyarzun from Universidad Andres Bello for X-ray diffraction measurements.

REFERENCES

(1) Liu, J.-L.; Chen, Y.-C.; Tong, M.-L. Symmetry Strategies for High Performance Lanthanide-Based Single-Molecule Magnets. *Chem. Soc. Rev.* **2018**, *47*, 2431−2453.

(2) Pointillart, F.; Cador, O.; Le Guennic, B.; Ouahab, L. Uncommon Lanthanide Ions in Purely 4f Single Molecule Magnets. *Coord. Chem. Rev.* **2017**, *346*, 150−175.

(3) McAdams, S. G.; Ariciu, A. M.; Kostopoulos, A. K.; Walsh, J. P. S.; Tuna, F. Molecular Single-Ion Magnets Based on Lanthanides and Actinides: Design Considerations and New Advances in the Context of Quantum Technologies. *Coord. Chem. Rev.* **2017**, *346*, 216−239.

(4) Bar, A. K.; Kalita, P.; Singh, M. K.; Rajaraman, G.; Chandrasekhar, V. Low-Coordinate Mononuclear Lanthanide Complexes as Molecular Nanomagnets. *Coord. Chem. Rev.* **2018**, *367*, 163−216.

(5) Zhu, Z.; Guo, M.; Li, X. L.; Tang, J. Molecular Magnetism of Lanthanide: Advances and Perspectives. *Coord. Chem. Rev.* **2019**, *378*, 350−364.

(6) Gómez-Coca, S.; Aravena, D.; Morales, R.; Ruiz, E. Large Magnetic Anisotropy in Mononuclear Metal Complexes. *Coord. Chem. Rev.* **2015**, *289*−*290*, 379−392.

(7) Sorace, L.; Benelli, C.; Gatteschi, D. Lanthanides in Molecular Magnetism: Old Tools in a New Field. *Chem. Soc. Rev.* **2011**, *40*, 3092−3104.

(8) Rinehart, J. D.; Long, J. R. Exploiting Single-Ion Anisotropy in the Design of f-Element Single-Molecule Magnets. *Chem. Sci.* **2011**, *2*, 2078−2085.

(9) Gonzalez, J. F.; Pointillart, F.; Cador, O. Hyperfine Coupling and Slow Magnetic Relaxation in Isotopically Enriched Dy^{III} Mononuclear Single-Molecule Magnets. *Inorg. Chem. Front.* **2019**, *6*, 1081−1086.

(10) Long, J.; Habib, F.; Lin, P.-H.; Korobkov, I.; Enright, G.; Ungur, L.; Wernsdorfer, W.; Chibotaru, L. F.; Murugesu, M. Single-Molecule Magnet Behavior for an Antiferromagnetically Superexchange-Coupled Dinuclear Dysprosium(III) Complex. *J. Am. Chem. Soc.* **2011**, *133*, 5319−5328.

(11) Ungur, L.; Chibotaru, L. F. Strategies toward High-Temperature Lanthanide-Based Single-Molecule Magnets. *Inorg. Chem.* **2016**, *55*, 10043−10056.

(12) Huang, C.-H. *Rare Earth Coordination Chemistry: Fundamentals and Applications*; John Wiley: Singapore, 2010.

(13) Ishikawa, N.; Sugita, M.; Wernsdorfer, W. Quantum Tunneling of Magnetization in Lanthanide Single-Molecule Magnets: Bis(Phthalocyaninato)Terbium and Bis(Phthalocyaninato)Dysprosium Anions. *Angew. Chem., Int. Ed.* **2005**, *44*, 2931−2935.

(14) Branzoli, F.; Carretta, P.; Filibian, M.; Zoppellaro, G.; Graf, M. J.; Galan-mascaros, J. R.; Fuhr, O.; Brink, S.; Ruben, M. Spin Dynamics in the Negatively Charged Terbium (III) Bis-Phthalocyaninato Complex. *J. Am. Chem. Soc.* **2009**, *131*, 4387−4396.

(15) Ishikawa, N.; Sugita, M.; Ishikawa, T.; Koshihara, S. Y.; Kaizu, Y. Lanthanide Double-Decker Complexes Functioning as Magnets at the Single-Molecular Level. *J. Am. Chem. Soc.* **2003**, *125*, 8694−8695.

(16) Gonidec, M.; Amabilino, D. B.; Veciana, J. Novel Double-Decker Phthalocyaninato Terbium(Iii) Single Molecule Magnets with Stabilised Redox States. *Dalton Trans.* **2012**, *41*, 13632−13639.

(17) Katoh, K.; Asano, R.; Miura, A.; Horii, Y.; Morita, T.; Breedlove, B. K.; Yamashita, M. Effect of f-f Interactions on Quantum Tunnelling of the Magnetization: Mono- and Dinuclear Dy(III) Phthalocyaninato Triple-Decker Single-Molecule Magnets with the Same Octacoordination Environment. *Dalton Trans.* **2014**, *43*, 7716−7725.

(18) Jiang, S.-D.; Wang, B. W.; Sun, H. L.; Wang, Z. M.; Gao, S. An Organometallic Single-Ion Magnet. *J. Am. Chem. Soc.* **2011**, *133*, 4730−4733.

(19) Jiang, S.-D.; Liu, S. S.; Zhou, L. N.; Wang, B. W.; Wang, Z. M.; Gao, S. Series of Lanthanide Organometallic Single-Ion Magnets. *Inorg. Chem.* **2012**, *51*, 3079−3087.

(20) Jeletic, M.; Lin, P.; Roy, J. J. L.; Korobkov, I.; Gorelsky, S. I.; Murugesu, M. An Organometallic Sandwich Lanthanide Single-Ion Magnet with an Unusual Multiple Relaxation Mechanism. *J. Am. Chem. Soc.* **2011**, *133*, 19286−19289.

(21) Le Roy, J. J.; Korobkov, I.; Murugesu, M. A Sandwich Complex with Axial Symmetry for Harnessing the Anisotropy in a Prolate Erbium(III) Ion. *Chem. Commun.* **2014**, *50*, 1602−1604.

(22) Singh, S. K.; Gupta, T.; Ungur, L.; Rajaraman, G. Magnetic Relaxation in Single-Electron Single-Ion Cerium(III) Magnets: Insights from Ab Initio Calculations. *Chem. - Eur. J.* **2015**, *21*, 13812−13819.

(23) Cucinotta, G.; Perfetti, M.; Luzon, J.; Etienne, M.; Car, P.; Caneschi, A.; Calvez, G.; Bernot, K.; Sessoli, R. Magnetic Anisotropy in a Dysprosium / DOTA Single-Molecule Magnet: Beyond Simple Magneto-Structural Correlations. *Angew. Chem., Int. Ed.* **2012**, *51*, 1606−1610.

(24) AlDamen, M. A.; Clemente-Juan, J. M.; Coronado, E.; Martí-Gastaldo, C.; Gaita-Ariño, A. Mononuclear Lanthanide Single-Molecule Magnets Based on Polyoxometalates. *J. Am. Chem. Soc.* **2008**, *130*, 8874−8875.

(25) AlDamen, M. A.; Cardona-Serra, S.; Clemente-Juan, J. M.; Coronado, E.; Gaita-Ariño, A.; Martí-Gastaldo, C.; Luis, F.; Montero, O. Mononuclear Lanthanide Single Molecule Magnets Based on the Polyoxometalates $[Ln(W_5O_{18})_2]^{9-}$ and $[Ln(\beta_2\text{-}SiW_{11}O_{39})_2]^{13-}$ (Ln^{III} = Tb, Dy, Ho, Er, Tm, and Yb). *Inorg. Chem.* **2009**, *48*, 3467−3479.
(26) Gavey, E. L.; Al Hareri, M.; Regier, J.; Carlos, L. D.; Ferreira, R. A. S.; Razavi, F. S.; Rawson, J. M.; Pilkington, M. Placing a Crown on Dy^{III} - A Dual Property Ln^{III} crown Ether Complex Displaying Optical Properties and SMM Behaviour. *J. Mater. Chem. C* **2015**, *3*, 7738−7747.
(27) Starynowicz, P. Two Complexes of Sm (II) with Crown Ethers — Electrochemical Synthesis, Structure and Spectroscopy. *Dalton Trans.* **2004**, 825−832.
(28) Petrosyants, S. P.; Ilyukhin, A. B. Ensembles of the Gallium, Indium, and Scandium Complexes with the Macrocycles. *Russ. J. Coord. Chem.* **2010**, *36*, 97−104.
(29) Hareri, M. Al.; Ali, Z. R.; Gavey, E. L.; Carlos, L. D.; Ferreira, R. A. S.; Pilkington, M. Dual-Property Supramolecular H - Bonded 15-Crown - 5 Ln(III) Chains: Joint Magneto-Luminescence and Ab Initio Studies. *Inorg. Chem.* **2017**, *56*, 7344−7352.
(30) Al Hareri, M.; Gavey, E. L.; Regier, J.; Ras Ali, Z.; Carlos, L. D.; Ferreira, R. A. S.; Pilkington, M. Encapsulation of a $[Dy(OH_2)_8]^{3+}$ Cation: Magneto-Optical and Theoretical Studies of a Caged, Emissive SMM. *Chem. Commun.* **2016**, *52*, 11335−11338.
(31) Ding, Y.-S.; Han, T.; Yue-Qiao, H.; Minwei, X.; Sen, Y.; Yan-Zhen, Z. Syntheses, Structures and Magnetic Properties of a Series of Mono- and Di- Nuclear Dysprosium(III)-Crown-Ether Complexes: Effects of Weak Ligand-Field and Flexible Cyclic Coordination Modes. *Inorg. Chem. Front.* **2016**, *3*, 798−807.
(32) Maxwell, L.; Amoza, M.; Ruiz, E. Mononuclear Lanthanide Complexes with 18-Crown-6 Ether: Synthesis, Characterization, Magnetic Properties, and Theoretical Studies. *Inorg. Chem.* **2018**, *57*, 13225−13234.
(33) Molton, F.; Maury, O.; Xémard, M.; Nocton, G.; Le Guennic, B.; Cador, O.; Cordier, M.; Duboc, C. Divalent Thulium Crown Ether Complexes with Field-Induced Slow Magnetic Relaxation. *Inorg. Chem.* **2019**, 2872−2880.
(34) Rousset, E.; Piccardo, M.; Boulon, M. E.; Gable, R. W.; Soncini, A.; Sorace, L.; Boskovic, C. Slow Magnetic Relaxation in Lanthanoid Crown Ether Complexes: Interplay of Raman and Anomalous Phonon Bottleneck Processes. *Chem. - Eur. J.* **2018**, *24*, 14768−14785.
(35) Ilyukhin, A.; Dobrokhotova, Z.; Petrosyants, S.; Novotortsev, V. Yttrium Thiocyanate-Based Supramolecular Architectures: Synthesis, Crystal Structures, and Thermal Properties. *Polyhedron* **2011**, *30*, 2654−2660.
(36) Mishra, S. Anhydrous Scandium, Yttrium, Lanthanide and Actinide Halide Complexes with Neutral Oxygen and Nitrogen Donor Ligands. *Coord. Chem. Rev.* **2008**, *252*, 1996−2025.
(37) Herchel, R.; Zoufalý, P.; Nemec, I. The Effect of the Second Coordination Sphere on the Magnetism of $[Ln(NO_3)_3(H_2O)_3]\cdot$(18-Crown-6) (Ln = Dy and Er). *RSC Adv.* **2019**, *9*, 569−575.
(38) *APEX2, SAINT and SADABS*; Bruker AXS Inc.: Madison, Wisconsin, USA, 2012.
(39) Sheldrick, G. M. A Short History of SHELX. *Acta Crystallogr., Sect. A: Found. Crystallogr.* **2008**, *64*, 112−122.
(40) Sheldrick, G. M. Crystal Structure Refinement with SHELXL. *Acta Crystallogr., Sect. C: Struct. Chem.* **2015**, *71*, 3−8.
(41) Westrip, S. P. PublCIF: Software for Editing, Validating and Formatting Crystallographic Information Files. *J. Appl. Crystallogr.* **2010**, *43*, 920−925.
(42) Neese, F. Software Update: The ORCA Program System, Version 4.0. *Wiley Interdiscip. Rev.: Comput. Mol. Sci.* **2018**, *8*, No. e1327.
(43) Becke, A. D. Density-Functional Exchange-Energy Approximation with Correct Asymptotic Behavior. *Phys. Rev. A* **1988**, *38*, 3098−3100.
(44) Perdew, J. P. Density-Functional Approximation for the Correlation Energy of the Inhomogeneous Electron Gas. *Phys. Rev. B* **1986**, *33*, 8822−8824.
(45) Weigend, F.; Ahlrichs, R. Balanced Basis Sets of Split Valence, Triple Zeta Valence and Quadruple Zeta Valence Quality for H to Rn: Design and Assessment of Accuracy. *Phys. Chem. Chem. Phys.* **2005**, *7*, 3297.
(46) Aravena, D.; Neese, F.; Pantazis, D. A. Improved Segmented All-Electron Relativistically Contracted Basis Sets for the Lanthanides. *J. Chem. Theory Comput.* **2016**, *12*, 1148−1156.
(47) Rösch, N.; Krüger, S.; Mayer, M.; Nasluzov, V. A. The Douglas-Kroll-Hess Approach to Relativistic Density Functional Theory: Methodological Aspects and Applications to Metal Complexes and Clusters. In *Recent Developments and Applications of Modern Density Functional Theory*; Seminario, J., Ed.; Elsevier, 1996; Vol. *4*, pp 497−566.
(48) Nakajima, T.; Hirao, K. The Douglas−Kroll−Hess Approach. *Chem. Rev.* **2012**, *112*, 385−402.
(49) Reiher, M. Relativistic Douglas−Kroll−Hess Theory. *Wiley Interdiscip. Rev.: Comput. Mol. Sci.* **2012**, *2*, 139−149.
(50) Malmqvist, P.-Å.; Roos, B. O. The CASSCF State Interaction Method. *Chem. Phys. Lett.* **1989**, *155*, 189−194.
(51) Aravena, D. Ab Initio Prediction of Tunneling Relaxation Times and Effective Demagnetization Barriers in Kramers Lanthanide Single-Molecule Magnets. *J. Phys. Chem. Lett.* **2018**, *9*, 5327−5333.
(52) Groom, C. R.; Bruno, I. J.; Lightfoot, M. P.; Ward, S. C. The Cambridge Structural Database. *Acta Crystallogr., Sect. B: Struct. Sci., Cryst. Eng. Mater.* **2016**, *72*, 171−179.
(53) Breneman, C. M.; Wiberg, K. B. Determining Atom-Centered Monopoles from Molecular Electrostatic Potentials. The Need for High Sampling Density in Formamide Conformational Analysis. *J. Comput. Chem.* **1990**, *11*, 361−373.
(54) Fock, V. Näherungsmethode Zur Lösung Des Quantenmechanischen Mehrkörperproblems. *Z. Phys.* **1930**, *61*, 126−148.
(55) Hartree, D. R. The Wave Mechanics of an Atom with a Non-Coulomb Central Field Part I Theory and Methods. *Math. Proc. Cambridge Philos. Soc.* **1928**, *24*, 89−110.
(56) Pollak, P.; Weigend, F. Segmented Contracted Error-Consistent Basis Sets of Double- and Triple - ζ Valence Quality for One- and Two-Component Relativistic All-Electron Calculations. *J. Chem. Theory Comput.* **2017**, *13*, 3696−3705.
(57) Glendening, E. D.; Badenhoop, J. K.; Reed, A. E.; Carpenter, J. E.; Bohmann, J. A.; Morales, C. M.; Karafiloglou, P.; Landis, C. R.; W, F. *NBO 7.0*; Theoretical Chemistry Institute, University of Wisconsin: Madison, 2018.
(58) Casanova, D.; Llunell, M.; Alemany, P.; Alvarez, S.; Cirera, J. *SHAPE*, Version 2.1; Universitat de Barcelona, 2013.
(59) Shiping, Y.; Zonghui, J.; Diazheng, L.; Genglin, W.; Ruji, W.; Honggen, W.; Xinkan, Y. Crystal Structure of the Complex of Dibenzo-30-Crown-10 with Dysprosium Isothiocyanate. *J. Inclusion Phenom. Mol. Recognit. Chem.* **1993**, *15*, 159−165.
(60) Bakker, J. M.; Deacon, G. B.; Forsyth, C. M.; Junk, P. C.; Wiecko, M. A Structural Investigation of Trivalent and Divalent Rare Earth Thiocyanate Complexes Synthesised by Redox Transmetallation. *Eur. J. Inorg. Chem.* **2010**, *2010*, 2813−2825.
(61) Martín-Ramos, P.; Silva, M. R. *Lanthanide-Based Multifunctional Materials From OLEDs to SIMs*; Elsevier Inc.: Amsterdam, Netherlands, 2018.
(62) Abragam, A.; Bleaney, B. *Electron Paramagnetic Resonance of Transition Ions*; Oxford University Press: Oxford, 1970.
(63) Aravena, D.; Ruiz, E. Shedding Light on the Single-Molecule Magnet Behavior of Mononuclear Dy^{III} Complexes. *Inorg. Chem.* **2013**, *52*, 13770−13778.
(64) Briganti, M.; Sessoli, R.; Garcia, G. F.; Jung, J.; Le, B.; Totti, F. Chemical Science Covalency and Magnetic Anisotropy in Lanthanide Single Molecule Magnets: The DyDOTA Archetype. *Chem. Sci.* **2019**, *10*, 7233−7245.
(65) Canaj, A. B.; Singh, M. K.; Wilson, C.; Rajaraman, G.; Murrie, M. Chemical and in Silico Tuning of the Magnetisation Reversal Barrier in Pentagonal Bipyramidal Dy(Iii) Single-Ion Magnets. *Chem. Commun.* **2018**, *54*, 8273−8276.

https://dx.doi.org/10.1021/acs.jpcc.9b09234
J. Phys. Chem. C 2020, 124, 5308−5320

(66) Echeverría, J.; Carreras, A.; Casanova, D.; Alemany, P.; Alvarez, S. Concurrent Symmetries: The Interplay Between Local and Global Molecular Symmetries. *Chem. - Eur. J.* **2011**, *17*, 359−367.

https://dx.doi.org/10.1021/acs.jpcc.9b09234
J. Phys. Chem. C 2020, 124, 5308−5320